A&A, 711, A280 (2026)
https://doi.org/10.1051/0004-6361/202660654

Astronomy & Astrophysics

Iron He-triplet signatures of shocks in the hottest galaxy clusters

Z/W line ratio, line broadening, and electron-ion temperature equilibration

Eugene Churazov[1,*], Yuri Ralchenko[2,3,4], Ildar I. Khabibullin[5,1], John C. Raymond[6], Annie Heinrich[7], Irina Zhuravleva[7], Reinout J. van Weeren[8], and Congyao Zhang[9,7]

[1] Max Planck Institute for Astrophysics, Karl-Schwarzschild-Str. 1, D-85741 Garching, Germany
[2] Department of Astronomy, University of Maryland, College Park, MD 20742, USA
[3] X-ray Astrophysics Laboratory, NASA Goddard Space Flight Center, Greenbelt, MD 20771, USA
[4] Center for Research and Exploration in Space Science and Technology, NASA Goddard Space Flight Center, Greenbelt, MD 20771, USA
[5] Rudolf Peierls Centre for Theoretical Physics, Department of Physics, University of Oxford, Clarendon Laboratory, Parks Rd, Oxford OX1 3PU, UK
[6] Center for Astrophysics | Harvard & Smithsonian, 60 Garden St., Cambridge, MA 02138, USA
[7] Department of Astronomy & Astrophysics, University of Chicago, Chicago, IL 60637, USA
[8] Leiden Observatory, Leiden University, PO Box 9513, 2300 RA Leiden, The Netherlands
[9] Department of Theoretical Physics and Astrophysics, Masaryk University, Brno 61137, Czechia

Received 28 April 2026 / Accepted 8 June 2026

ABSTRACT

A merger of clusters naturally drives shocks with Mach number $\mathcal{M} \lesssim 3$ in the intracluster medium (ICM). This process creates several distinct signatures, including sharp surface-brightness "edges", temperature, and gas-velocity jumps. The low density of the ICM implies that ionization balance and electron-ion equilibration timescales can be long enough to produce additional observable signatures. Here, we focus on two "transient" spectral signatures accessible with high-energy-resolution telescopes such as *XRISM*, even in unfavorable geometries, for example when we are looking inside the Mach cone of the shock, which precludes the appearance of sharp edges in X-ray images. In this work, we focus on (i) the Z/W line ratio of the Fe XXV triplet and (ii) the contribution of ions with $T_i > T_e$ to the line width, which might be mistakenly interpreted as gas turbulence. We demonstrate that the Z/W ratio can serve as a proxy for the nonequilibrium state of the shocked ICM and facilitate interpretation of the line broadening. We conclude that these spectral signatures are within reach of missions such as *XRISM* and can be used to constrain the electron heating at collisionless cluster shocks, as well as the rate of subsequent temperature equilibration between different particle species.

Key words. atomic processes – line: formation – line: profiles – shock waves – galaxies: clusters: intracluster medium

1. Introduction

Cluster mergers are common in cosmological simulations and observations. Minor mergers, in which one of the merging clusters is much less massive than the other, are very frequent, whereas equal-mass mergers are rarer. The latter often lead to spectacular features that reveal the physics of the merger process (see e.g. Markevitch & Vikhlinin 2007, for a review). The ICM temperature in galaxy clusters scales with the mass as $T_X \propto GM_v/R_v \sim V_v^2$, where the subscript "v" denotes characteristic virial quantities. Since the sound speed and the virial velocity follow the same scaling with mass, one expects a similar range of shock Mach numbers, independent of the cluster mass. For a Navarro-Frenk-White potential with a concentration parameter of $c \sim 2$–6 (e.g., Comerford & Natarajan 2007), the velocity of a point mass on a parabolic trajectory reaches $\sim$3.05–3.3V_v in the cluster center. This sets a natural characteristic value for the maximal Mach number, $\mathcal{M} \lesssim 3$, expected during pericenter passage. We discuss a generic case throughout the text, with examples such as the Bullet cluster (Markevitch et al. 2002) and the Peanut cluster (Lyskova et al. 2025) in mind. For illustration, we assume an initial gas temperature of 7 keV (for $M_v \sim 10^{15}\,M_\odot$) and a shock with $\mathcal{M} = 3.2$.

In the context of cluster shocks, the ICM density can be very low ($n_e \sim 10^{-3}$–$10^{-4}\,\mathrm{cm}^{-3}$), implying that the relaxation timescales can be on the order of 10^8 yr, and departures from ionization equilibrium or different temperatures of electrons and ions might persist long enough to produce observable signatures (e.g., Fox & Loeb 1997; Chièze et al. 1998; Takizawa 1999; Markevitch & Vikhlinin 2007; Wong & Sarazin 2009; Akahori & Yoshikawa 2010; Russell et al. 2012; Di Mascolo et al. 2019; Sarkar et al. 2024; Norseth et al. 2025). A similar set of processes defines the properties of heated plasma in supernova-remnant shocks in the interstellar medium (ISM) (e.g., Bykov et al. 2008; Vink 2012; Raymond et al. 2023). However, unlike the ISM, the ICM is hot, except in the very outskirts, and the sonic Mach number $\mathcal{M}$ is typically not much larger than three. Another difference is that most of the ICM has plasma $\beta = \frac{P_{\mathrm{ICM}}}{B^2/8\pi} \approx 100$, where P_{ICM} is the ICM thermal pressure and B is the magnetic field; therefore, the Alfven Mach number is larger, $\mathcal{M}_A = \beta^{1/2}\mathcal{M} \sim 10\mathcal{M}$.

The He-like triplet diagnostic is one of the powerful probes of low-density hot collision-dominated plasma (e.g.,

* Corresponding author: churazov@mpa-garching.mpg.de

Porquet et al. 2001). The most prominent lines are normally the well-separated resonance W ($1s^2\ ^1S_0 - 1s2p\ ^1P_1$) line and the forbidden magnetic-dipole Z ($1s^2\ ^1S_0 - 1s2s\ ^3S_1$) line, while the intercombination Y ($1s^2\ ^1S_0 - 1s2p\ ^3P_1$) and magnetic-quadrupole X ($1s^2\ ^1S_0 - 1s2p\ ^3P_2$) lines are often blended by dielectronic satellites. The non-equilibrium ionization (NEI) signatures associated with the He-like triplet of high-Z elements have long been considered in the literature (e.g., Mewe & Schrijver 1978; Liedahl 1999; Oelgoetz & Pradhan 2004). Here, we discuss these effects for an idealized case of a plane-parallel shock in the ICM, bearing in mind the capabilities of X-ray calorimeters such as the *XRISM* observatory (Tashiro et al. 2025), to complement merger signatures with high-resolution spectroscopic information.

We consider two models in the next section.

The first model assumes that the downstream temperatures of all species are equal immediately after the shock, and only the ionization balance evolves with time. A parameter $\tau = n_e t \sim 10^{12}\ \mathrm{cm^{-3}\ s}$, where n_e is the electron density, sets the characteristic timescale t for NEI effects in this model, in particular, deviations of the relative line strengths from the collisional ionization equilibrium (CIE) predictions for the electron temperature measured from the shape of the continuum spectrum.

In the second model, the electrons and ions have different temperatures downstream of the shock and gradually equilibrate via Coulomb collisions. In this model,

- electrons are heated adiabatically, while ions undergo adiabatic heating and are additionally heated in proportion to their mass. Beyond the NEI effects, line widths are then governed by the different ion temperatures;
- ions first equilibrate with each other, lowering their temperatures to the proton temperature on a timescale similar to that of ionization equilibrium;
- electrons equilibrate with protons (and other ions) on a timescale approximately ten times longer than ion-proton equilibration, with the ionization equilibrium evolving along with the electron temperature, while the thermal broadening of ions follows the proton temperature.

2. Model

2.1. Relevant physical processes

As an illustrative example, we consider a hot plasma with an initial temperature $T_0 = 7$ keV. In the initial state, the electron and ion temperatures are equal ($T_e = T_i$), and the plasma is in the state of CIE corresponding to this temperature[1]. The plasma is optically thin, and the level population corresponds to the coronal approximation. A plane-parallel collisionless shock with $\mathcal{M} = 3.2$ instantly changes the density and the mean plasma temperature according to the Rankine-Hugoniot conditions for the adiabatic index $\gamma = 5/3$. For $\mathcal{M} = 3.2$, the density and temperature jumps are $\rho_{\rm ds} \approx 3.09\rho_0$ and $T_{\rm ds} \approx 4.06T_0$, with the subscript "ds" denoting downstream of the shock.

2.2. Electron-ion temperature equilibration

For the downstream temperatures of different species, we consider two cases:

- A: $T_e = T_p = T_Z = T_{\rm ds}$ for all species.
- B: $T_e \neq T_p \neq T_Z$ and pure Coulomb collisions control the temperature equilibration.

In the second case, we set the initial temperatures to be "maximally different". Namely, we assume that ion temperatures, in addition to adiabatic heating, scale with the ion masses $T_i \propto m_i$, while the initial electron temperature corresponds to the adiabatic compression set by the density jump, such that $T_{e,\rm ds} = T_0(\rho_{\rm ds}/\rho_0)^{(\gamma-1)} \approx 2.12T_0$ (for a compression ratio of 3.09). This assumption corresponds to the limit in which each particle species thermalizes a fraction of the shock speed independently, without any energy exchange between particle species. It may occur in collisionless shocks, where the shock transition is mediated by plasma turbulence and electromagnetic fields instead of collisions between particles (see, e.g. Ghavamian et al. 2007; Bykov et al. 2008; Vink et al. 2015; Raymond et al. 2017, and references therein). With this definition, electrons, protons, and Fe XXV ions have the following temperatures immediately downstream: $T_{e,\rm ds} \approx 15$ keV, $T_{p,\rm ds} \approx 43$ keV, and $T_{\rm Fe,ds} \approx 1.5$ MeV, respectively. Unlike high-Mach-number shocks in young supernova remnants (Ghavamian et al. 2013; Raymond et al. 2023), where the $T_{e,\rm ds}/T_{p,\rm ds}$ ratio can be very low (under the same assumptions), in clusters this ratio is modest by virtue of the limited sonic Mach number, so that the adiabatically heated electrons are only a factor of $\lesssim 3$ colder than protons. The adiabatic heating of electrons at ICM shocks is also supported by observations (e.g., Russell et al. 2022; Sarkar et al. 2024; Norseth et al. 2025).

Subsequent evolution of the temperatures in case B can be reasonably accurately described by coupling between electrons and protons, and between ions and protons, namely

$$\frac{\mathrm{d}T_e}{\mathrm{d}t} = \nu_{\rm ep} n_p (T_p - T_e) \tag{1}$$

$$\frac{\mathrm{d}T_p}{\mathrm{d}t} = \nu_{\rm ep} n_e (T_e - T_p) \tag{2}$$

$$\frac{\mathrm{d}T_Z}{\mathrm{d}t} = \nu_{Ze} n_e (T_e - T_Z) + \nu_{Zp} n_p (T_p - T_Z), \tag{3}$$

where $n_{\rm e}$, $n_{\rm p}$, and n_Z are the number densities of electrons, protons, and heavy ions, respectively; the ν_{ab} terms define the rates of energy exchange between two species, a and b (Spitzer 1962). A more accurate treatment would include helium and coupling between all species. We show this in Appendix C. However, for our illustrative example, the three equations above are sufficient. The first two describe the energy exchange between electrons and protons. Heavy ions are not important in the overall energy budget due to their low abundance. Therefore, we can trace their temperature evolution through collisions with electrons and protons (the third equation), but we can ignore their back-reaction on other species. Since we ignore the impact of He, it would be logical to ignore the first term on the right-hand side of the third equation, which is subdominant compared to the rate of energy exchange between iron and helium ions. We keep it to maintain a self-consistent approximation in which all ions heavier than a proton (by assumption) make a negligible contribution to the total energy density. As we illustrate in Appendix C, this is sufficient for typical applications, unless very accurate predictions are required.

The evolution of $T_{\rm e}$, $T_{\rm p}$, and T_Z in our illustrative model is shown in Fig. 1. As expected, for pure Coulomb collisions, T_Z approaches $T_{\rm p}$ on a timescale $t_{Z,p}$, which is an order of magnitude shorter than that of the electron-ion equilibration. The corresponding value of $\tau_{Z,p} = t_{Z,p} n_e \approx t_{Z,p} n_p \lesssim 10^{12}\ \mathrm{cm^{-3}\ s}$, while $\tau_{e,p} \sim 10^{13}\ \mathrm{cm^{-3}\ s}$. As shown in the following (Sect. 2.3), the

[1] We used T_i for the temperature of any ion, including protons. When needed, we used $T_{\rm p}$ for protons and T_Z for ions of high-Z elements such as iron.

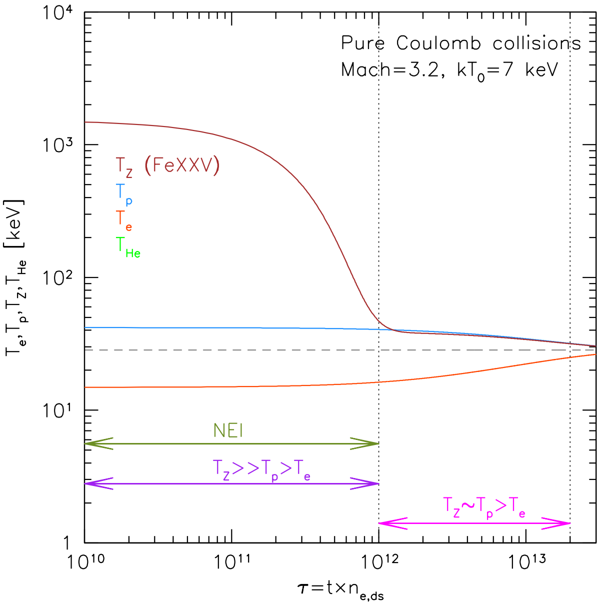

Fig. 1. Coulomb-collision-mediated temperature equilibration between electrons, protons, and He-like iron ions (Fe XXV) in the limit of adiabatic heating of electrons at the shock. The Fe XXV ions temperature, T_Z, approaches $T_{\rm p}$ at $\tau \sim 10^{12}\,{\rm cm}^{-3}\,{\rm s}$ and then evolves together with $T_{\rm p}$. The NEI timescale (see Fig. 2 below) is approximately the same as the $T_Z \gg T_{\rm p}$ timescale. Ions remain hotter than electrons up to $\tau \sim 2$–$3 \times 10^{13}\,{\rm cm}^{-3}\,{\rm s}$. Therefore, the Fe XXV ions are hotter than $T_{\rm e}$ up to this value of τ, and the thermal broadening of the Fe XXV lines is larger than that predicted from the electron temperature $T_{\rm e}$ derived from the continuum shape. The helium abundance is set to zero for this plot (see Fig. C.1 for the impact of helium).

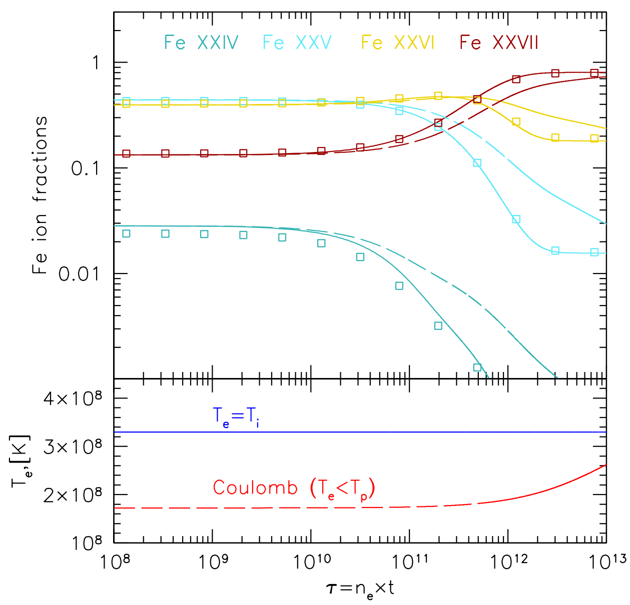

Fig. 2. Ionization balance and temperature evolution in the shocked medium. *Bottom*: Evolution of $T_{\rm e}$. The solid blue line corresponds to the $T_e = T_i$ = const case, while the dashed red line shows the "Coulomb" temperature equilibration, with T_e initially set by adiabatic compression in the $\mathcal{M} = 3.2$ shock. In this case, $T_{\rm e}$ rises slowly and does not reach $T_{\rm p}$ even at $\tau = 10^{12}\,{\rm cm}^{-3}\,{\rm s}$. *Top*: Evolution of ionization balance. Solid lines show the $T_e = T_i$ case, based on `CHIANTI` rates, and open squares show the `NOMAD` results. Dashed lines show the ion fraction evolution when the electron temperature itself evolves with time, as shown in the bottom panel.

typical value of $\tau_{\rm CIE}$ required to establish the ionization equilibrium is on the same order as $\tau_{Z,p}$ and is smaller than $\tau_{e,p}$. This implies that for $\tau \gtrsim 10^{12}\,{\rm cm}^{-3}\,{\rm s}$, the ion fractions are close to CIE and follow the $T_e(t)$ evolution. The observed spectra (for these values of τ) can therefore be represented as a superposition of CIE spectra with different plasma temperatures. However, the thermal line width of the ions is set by T_Z, which can be larger than T_e up to $\tau \sim 10^{13}\,{\rm cm}^{-3}\,{\rm s}$. Therefore, the measured line width may be erroneously attributed to turbulence if only iron lines are observed (at least two elements with different masses are required to differentiate turbulence from thermal broadening). We return to this issue in Sect. 3.2.

We note that Coulomb collisionality is unlikely to govern all equilibration processes in the ICM. Magnetic fields can effectively increase the rate of ion-electron collisions via scattering from plasma instabilities (Schekochihin & Cowley 2006) or anisotropic transport along field lines (Kunz et al. 2011). A reduced effective viscosity below the Coulomb level has been detected in the ICM via the suppression of Kelvin-Helmholtz instabilities in cold fronts (e.g., Markevitch & Vikhlinin 2007; Zuhone & Roediger 2016) and via the extension of density fluctuations power spectra into the viscous regime (Zhuravleva et al. 2019; Heinrich et al. 2024). Thus, the actual isotropisation rate is likely to lie somewhere between cases A and B. However, this does not necessarily mean that the temperature equilibration rate is also enhanced, since the latter requires the transfer of energy from heavier to lighter particles (from ions to electrons) rather than the randomization of particle velocities and momentum exchange.

2.3. NEI and the He-like triplet

To study the time-varying ionization balance and line intensities, we used two collisional-radiative models, namely, the `CHIANTI` database (Dere 2007; Del Zanna et al. 2021) and the `NOMAD` code (Ralchenko & Maron 2001; see Appendix for more details). As shown in the following, good agreement between two independent sets of simulations provides extra confidence in the derived results.

The top panel of Fig. 2 shows the time evolution of the iron ion fractions (Fe XXIV–XXVII). The solid lines (`CHIANTI`) and open squares (`NOMAD`) correspond to the case $T_e = T_i$, while the dashed lines illustrate the case in which the electron temperature evolves in time due to Coulomb collisions.

The impact of nonequilibrium ionization on the line ratios has long been recognized (e.g., Mewe & Schrijver 1978; Liedahl 1999), in particular for conditions relevant to solar flares and laboratory plasmas. In these studies, the initial temperatures were typically low, and Li-like ions played a particularly important role once the temperature increased suddenly, driving the `Z/W` flux ratio above the characteristic CIE values. In contrast, in massive, high-temperature clusters, the fraction of Li-like iron ions is lower in the initial state, and the increased rate of inner-shell ionizations of these ions (contributing to the `Z` line) remains subdominant to the increased rate of Fe XXV collisional excitations populating the `W` line. Table B.1 lists the key properties of the Fe XXV triplet and Fe XXVI Lyα doublet lines.

Fig. 3 illustrates the impact of the instantaneous change in electron temperature from T_0 to T_1 on the `Z/W` line intensity ratio. In this regime, the ionization balance corresponds to CIE at temperature T_0, while the electron temperature is T_1. The top-left corner corresponds to $T_1 > T_0$ scenario, e.g., a shock, while the

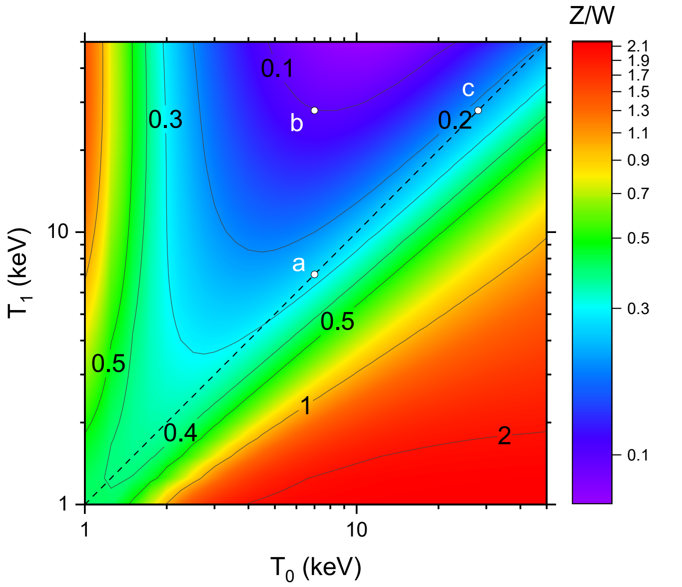

Fig. 3. Simulated `Z/W` line intensity ratio (colors; `NOMAD` simulation) for an instantaneous change in electron temperature from T_0 to T_1 in the limit of small τ. Locations a and c correspond to the flux ratios for the initial and final states with $T = 7$ keV and $T = 28$ keV, respectively. The dashed diagonal line shows the locus of other equilibrium states with $T_1 = T_0$. Location b corresponds to the intermediate case with $T_0 = 7$ keV, $T_1 = 28$ keV, and $\tau = 10^{10}\,\mathrm{cm^{-3}}$ s. A similar ratio is expected over a wide range of $\tau \lesssim 3\times10^{10}\,\mathrm{cm^{-3}}$ s. This transient state with an anomalously low `Z/W` ratio may serve as a signature of freshly shocked hot NEI plasma.

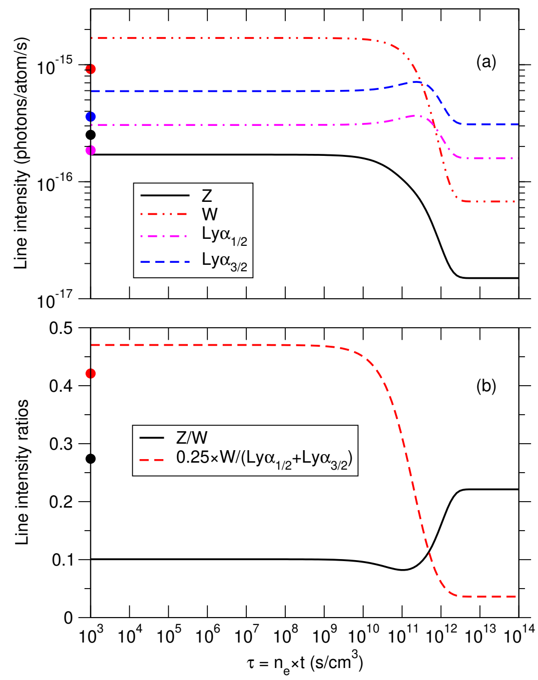

Fig. 4. Time-dependent (a) line intensities and (b) line intensity ratios for He- and H-like Fe from the `NOMAD` simulation ($T_0 = 7$ keV, $T_1 = 28$ keV, $T_e = T_p$ case). The 0.25 scaling factor applied to the W/Lyα ratio places all data on the same scale. Solid circles show the corresponding values at $\tau = 0$, i.e., $T_0 = 7$ keV.

bottom-right corresponds to the $T_1 < T_0$ case, e.g., fast expansion. The former regime leads to a decrease in the `Z/W` ratio, while the latter pushes the ratio in the opposite direction.

Fig. 4 shows the evolution of the `Z/W` flux ratio as a function of the ionization parameter τ for our fiducial model. We produced the ratios with `NOMAD` following the procedure described in the Appendix. As explained therein, during the NEI "frozen ionization balance phase" at $\tau \lesssim 10^{10}\,\mathrm{s/cm^3}$ the `Z/W` flux ratio is governed by several factors, such as ion populations and modified rate coefficients for electron-impact processes.

2.4. He-like versus H-like

Another useful and currently accessible diagnostic is the ratio of the Fe XXVI Ly$_\alpha$ and Fe XXV triplet fluxes. Under CIE conditions, this ratio serves as a line-based temperature proxy. Studies have also considered the NEI aspects of this flux ratio (e.g., Prokhorov 2010; Inoue et al. 2016). For our baseline model with a rather hot ICM, the Boltzmann factor ($e^{-\Delta E/kT}$) is already close to unity ($\Delta E \ll kT$), and the flux ratio is mostly driven by changes in the iron ionization fractions, from the He-dominated state at the beginning to the H-dominated state at large τ. This is illustrated by dashed lines in Fig. 4. Fig. 5 shows a comparison of the line ratios for the $T_e = T_i$ and evolving T_e cases. This figure also illustrates the impact of the shock strength (Mach numbers of 3.2 and 1.8) on the magnitude of the effect. Qualitatively, suppression of the `Z/W` ratio is always present, although a factor of three decreases requires a shock with $\mathcal{M} \gtrsim 3$.

The key role of NEI effects in the Ly$_\alpha$/`W` ratio is that, due to time-dependent changes in the ionization fractions, this ratio can take different values for the same electron temperature derived from the continuum shape. This provides additional flexibility in describing spectra in merging clusters and can itself serve as evidence for recently shocked gas in the system.

We note in passing that none of the nonstationary effects considered in this study directly affects the ratio of the Ly$_\alpha$ doublet components in Fe XXVI. In the `NOMAD` calculations, this ratio (Ly$\alpha_{3/2}$/Ly$\alpha_{1/2}$) is 1.94 (or 1.8 if a contribution of 1s–2s M1 transitions is taken into account) and is about the same upstream and downstream of the shock. Therefore, the anomalies reported in XRISM Collaboration (2025) remain unexplained. Finite (and different) optical depths of the two components can modify the flux ratio, suppressing more the Ly$\alpha_{3/2}$ if the scattering "screen" lies between the bright core and the observer (see examples in Churazov et al. 2010). In particular, a configuration with a velocity offset of $\sim$900 km s^{-1} between the emitting and scattering materials might result in the red-shifted Ly$\alpha_{3/2}$ line falling in resonance with the Ly$\alpha_{1/2}$ transition and undergoing stronger scattering (as in the case considered in Khabibullin & Sazonov 2012). However, the estimated Coma optical depth in these lines is small (e.g., Sazonov et al. 2002) and does not resolve the anomaly (XRISM Collaboration 2025). We also note that, given sufficiently high photon-count statistics, the ratio of the Fe XXV Kβ to Fe XXV Kα–`W` line can be used to estimate possible suppression of the resonant component, since this ratio is virtually insensitive to the ionization state and electron temperature of the plasma when $kT_e \gg E_{K\beta} - E_W \approx 1$ keV.

2.5. Line broadening

The broadening of the Fe XXV and Fe XXVI lines is a direct proxy of ion motions. It can be subdivided into thermal motions of individual ions and macroscopic plasma motions. Since the thermal velocity scales as $(\frac{T_Z}{m_Z})^{1/2}$, where $m_Z \approx 2Zm_\mathrm{p}$ is the ion mass, the contribution of thermal motions to the line width is the

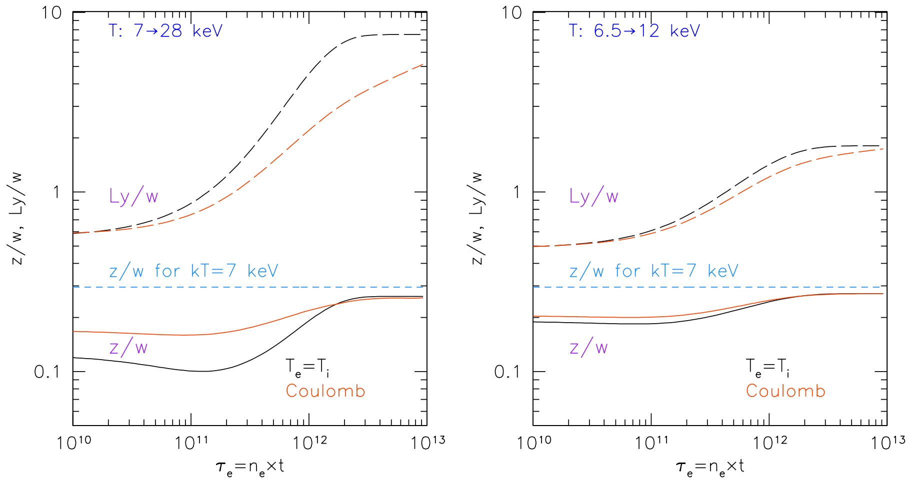

Fig. 5. *Left*: Evolution of Z/W (solid lines) and Ly/W (dashed lines) ratios following an instantaneous (black) and Coulomb-collisions-mediated (red) increase in electron temperature from 7 to 28 keV (corresponding to $\mathcal{M} = 3.2$ shock). The dashed blue line shows the ratio for a $kT = 7$ keV CIE plasma. *Right*: Same as in the left panel but for an initial temperature of 6.5 keV and a final temperature of 12 keV (corresponding to a $\mathcal{M} = 1.8$ shock). While the Z/W flux ratio differs between the $T_e = T_\mathrm{p}$ and $T_e < T_\mathrm{p}$ cases, it remains lower than the CIE-predicted values. The evolution of the Ly/W ratio is driven primarily by time-dependent changes in the ionization balance.

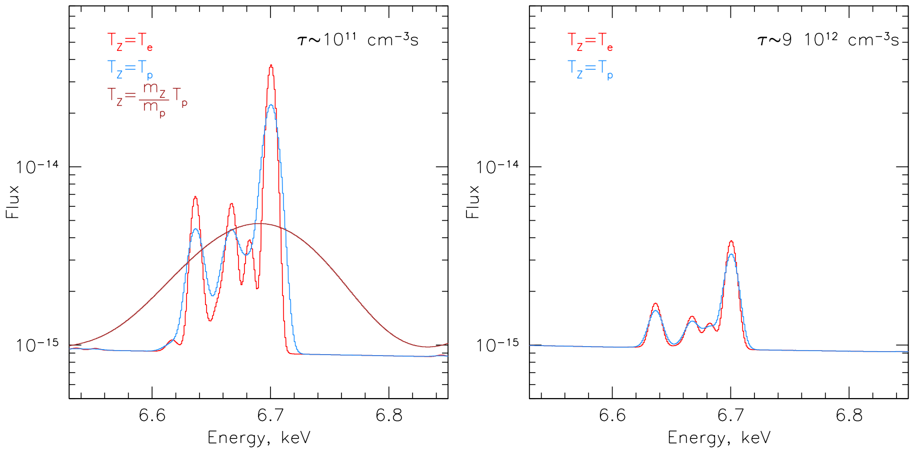

Fig. 6. Triplet spectrum for different assumptions about the ion temperature and different ionization parameter τ. *Left*: Case with $\tau = 10^{11}\,\mathrm{cm^{-3}}$ s. The red, blue, and brown curves show $T_Z = T_\mathrm{e}$, $T_Z = T_\mathrm{p}$, and $T_Z = \frac{m_Z}{m_p} \approx 2Z \times T_\mathrm{p}$ in a shocked plasma with pure Coulomb energy exchange between species. *Right*: Case with $\tau = 9 \times 10^{12}\,\mathrm{cm^{-3}}$ s. For this value of τ, $T_Z = T_\mathrm{p}$, but it remains larger than T_e, leading to marginally broader lines. For these large values of τ, the ionization fractions trace the time evolution of T_e, while the ion temperature tracks T_p. As a result, XSPEC reproduces the triplet fluxes for the $T_Z = T_\mathrm{p}$ case (blue line) with the BAPEC model using $kT = 22$ keV (instead of 28 keV) and an extra Gaussian velocity broadening of $\sigma = 180\,\mathrm{km\,s^{-1}}$. The $T_Z = T_\mathrm{e}$ model (red line) is reproduced with the BAPEC model using $kT = 22$ keV and no velocity broadening.

smallest for heavy ions, which therefore provides the best constraints on the ICM velocities. Most often, CIE conditions are assumed and $T_Z = T_\mathrm{e}$. This allows the temperature to be constrained from the broad-band X-ray spectrum and the line ratios, predicts pure thermal broadening, and determines the additional velocity broadening needed to describe the observed line width. However, these assumptions may not be valid downstream of the shock. As shown in Fig. 1, the temperature of iron ions can be higher than the electron temperature for $\tau \lesssim 10^{13}\,\mathrm{cm^{-3}}$ s, while for $\tau \lesssim 10^{11}\,\mathrm{cm^{-3}}$ s, even the CIE assumption is not valid. Figure 6 illustrates these cases for our fiducial model with pure Coulomb collisions and no plasma bulk motions. In reality, supersonic bulk motions contributing to the observed line width must be present in the shock scenario unless the normal to the shock front lies exactly in the plane of the sky. Essentially, the excess line broadening (e.g., in the $T_Z \propto m_Z T_\mathrm{p}$ scenario) results from isotropisation of the ion velocity jump at the shock front. Therefore, correct interpretation of the observed line broadening requires knowledge of the flow geometry.

3. Discussion

3.1. Nonequilibrium versus equilibrium emission measure

We first performed an order-of-magnitude comparison of the contribution of shocked gas to X-ray spectra with that of unshocked gas. Specifically, we are interested in regions with a characteristic ionization parameter τ comparable either to the NEI scale or to the $T_e \neq T_\mathrm{p}$ scale. We considered a planer shock viewed along the normal to the shock front. The downstream density and velocity are $\rho_\mathrm{ds} = C\rho_0$ and $v_\mathrm{ds} = v_\mathrm{s}/C$, where C is the compression factor. The length l_τ of the downstream region with the ionization parameter smaller than τ is

$$l_\tau = \frac{\tau}{\rho_\mathrm{ds}} v_\mathrm{ds} = \frac{\tau}{\rho_0 C}\frac{v_\mathrm{s}}{C}. \quad (4)$$

Therefore, the line-of-sight-integrated emission measure of this region is

$$\mathrm{EM}_\tau = l_\tau (\rho_0 C)^2 = v_\mathrm{s}\tau\rho_0. \quad (5)$$

This value can be compared with the cluster emission measure along the line of sight,

$$\mathrm{EM}_\mathrm{cl} \sim \rho_0^2 R_\mathrm{cl}, \quad (6)$$

where R_cl is the characteristic size of the region that dominates X-ray emission. Thus, the ratio

$$\frac{\mathrm{EM}_\tau}{\mathrm{EM}_\mathrm{cl}} = \frac{v_\mathrm{s}\tau}{\rho_0 R_\mathrm{cl}} \quad (7)$$

determines the relative contributions of the nonequilibrium part of the shock-heated gas to the total cluster flux. For a typical cluster density profile, the distance from the cluster center r can be used as $R_{\rm cl}$. Furthermore, the quantity $\rho_0 R_{\rm cl} \sim \rho(r) r$ indicates where in the cluster the impact of the shock is expected to be strongest. This is illustrated in Fig. 7. There, we set $v_{\rm s} = v_{\rm r}$, the velocity of a particle on a parabolic orbit in the NFW potential. We also set $\rho(r)$ to the mean density profile of the simulated clusters from O'Neil et al. (2021). Observationally, finding examples of clusters in which the shock crosses the center is challenging, since this phase is short-lived (see, however, Lyskova et al. 2025, for examples of merging clusters close to the pericenter passage). It is also difficult to obtain detailed spectra from cluster outskirts with the current generation of X-ray telescopes due to the very low gas density and hence low flux. Therefore, the most promising are the intermediate regions within R_{500c}. As is clear from Fig. 7, the contribution of the shock-heated gas at these radii is ~10% for $\tau \lesssim 10^{11}$ cm^{-3} s and of order unity for $\tau \lesssim 10^{12}$ cm^{-3} s. Compared with Fig. 1, we conclude that under favorable conditions the contribution of the shock can be large enough to produce observable spectral signatures associated with the ionization parameter $\tau \sim 10^{11}$ cm^{-3} s.

3.2. Diagnostic

The baseline spectral model used to describe emission from galaxy clusters is the optically thin thermal plasma emission model in CIE. The second commonly used model is a two-temperature CIE model that accounts for plasma with different temperatures observed along the same line of sight. The features associated with deviations from the ionization or electron-ion temperature equilibria might not be adequately captured by the two-temperature model. As discussed in Sect. 2, there are two characteristic values of τ, which are associated with specific nonequilibrium features in the X-ray spectra. Namely,

1. For $\tau \lesssim 10^{12}$ cm^{-3} s, the Z/W ratio in the Fe XXV triplet can be anomalously low due to NEI effects (see Fig. 3).
2. For $\tau \lesssim 10^{12}$ cm^{-3} s, Fe line broadening can be extremely high due to the higher temperature of massive ions in the absence of efficient ion-proton temperature equilibration (see the left panel of Fig. 6).
3. For $\tau \lesssim 10^{13}$ cm^{-3} s, Fe line broadening can be greater than the thermal broadening corresponding to the observed electron temperature in the regime, when $T_i = T_p > T_{\rm e}$, in the absence of efficient electron-proton temperature equilibration (see the right panel of Fig. 6).

The first item in the above list is associated with the ionization timescale of He-like ions and should be present even if $T_e = T_i = T_{\rm p}$ (see Fig. 1). The broadening (items 2 and 3), on the contrary, strongly depends on the initial temperatures of different species immediately downstream of the shock and on the efficiency of subsequent temperature equilibration. As discussed in Sect. 2.5, the ability to differentiate contributions from ICM motions and ion thermal motions downstream of the shock requires explicit knowledge of the shock geometry or a shock model.

Observationally, supernova remnant shocks show ion temperatures that are mass-proportional in high Mach number shocks but near equilibration in lower Mach number shocks (Raymond et al. 2017). Shocks in the solar wind show a large scatter in the ratio of $T_i/T_{\rm p}$ (Korreck et al. 2007), but T_i is generally greater than $T_{\rm p}$. Particle-in-cell (PIC) simulations show nearly mass-proportional thermal core temperatures for He and CNO in a $\mathcal{M} = 40$ shock (Caprioli et al. 2025). Observations of shocks in supernova remnants indicate fairly complete electron-ion equilibration at low Mach numbers, but $T_{\rm e}$ is only a few percent of $T_{\rm p}$ at high Mach numbers (Vink 2012; Ghavamian et al. 2013; Yamaguchi et al. 2014; Raymond et al. 2023). Solar wind shocks show the same general trend but with large scatter (Wilson et al. 2020), and $T_{\rm e}/T_{\rm p}$ appears to rise slowly at high Mach numbers in both PIC simulations and solar wind shocks (Bohdan et al. 2020; Hanusch et al. 2020; Tsiolis et al. 2021).

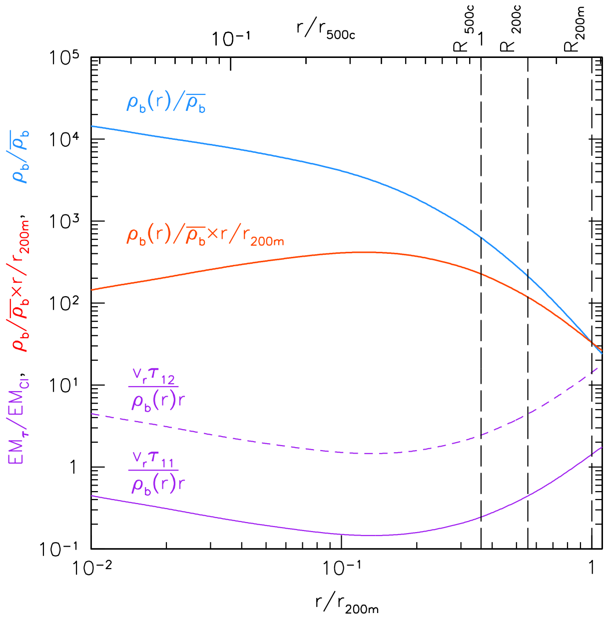

Fig. 7. Emission measure EM_τ of shocked gas with the ionization parameter τ below a given threshold, relative to the emission measure $\mathrm{EM}_{\rm cl}$ of unshocked gas at the same distance from the cluster center (see Eq. 7). The solid and dashed purple lines show the ratio $\mathrm{EM}_\tau/\mathrm{EM}_{\rm cl}$ for $\tau = 10^{11}$ and 10^{12} cm^{-3} s, respectively. For the shock velocity, we use the velocity v_r of a point mass on a parabolic orbit. The blue and red lines show the overdensity of baryons as a function of radius and the product of overdensity and radius, respectively. The reciprocal of the latter quantity is the key quantity that determines the ratio $\mathrm{EM}_\tau/\mathrm{EM}_{\rm cl}$. The plots show that regions with $\tau \sim 10^{11}$ cm^{-3} s can contribute ~10% to the line-of-sight emission measure, while for $\tau \sim 10^{12}$ cm^{-3} s the contributions from shocked and unshocked regions can be comparable. This conclusion holds for essentially any projected distance from the cluster center, although projection effects may also play a role.

3.3. Radio-guided selection of potential NEI sites

Identifying regions that may exhibit departures from ionization equilibrium or differences between electron and ion temperatures benefits from accurate knowledge of the shock-front location. However, detecting shocks in X-ray observations is often challenging due to low surface brightness and projection effects. Radio relics are arc-like polarized structures that extend up to 1–2 Mpc in galaxy clusters and are widely interpreted as tracers of shock fronts (for a review see van Weeren et al. 2019). At these locations, nonthermal particles are (re)accelerated into a power-law energy distribution (e.g., Drury 1983; Loi et al. 2017; Rajpurohit et al. 2020) and are subsequently advected downstream of the shock, where they cool on characteristic timescales given by

$$t_{\rm cool}[{\rm yr}] = 1.0 \times 10^9 \, \frac{B_{\mu{\rm G}}^{1/2}}{B_{\mu{\rm G}}^2 + B_{{\rm CMB},\mu{\rm G}}^2} \left[(1+z)\nu_{\rm GHz}\right]^{-1/2}, \qquad (8)$$

with the observed radio frequency $\nu_{\rm GHz}$ in GHz, magnetic field strengths $B_{\mu{\rm G}}$ and $B_{{\rm CMB},\mu{\rm G}}$ in μGauss, and z being the cluster redshift. Here, $B_{\rm CMB} \approx 3.25 \times (1+z)^2$ μG is set by the condition that $B^2_{\rm CMB}/8\pi$ is equal to the CMB energy density at redshift z.

This cooling leads to a progressive steepening of both the electron energy distribution and the observed radio spectrum over a characteristic length scale of $t_{\rm cool} v_{\rm ds}$. For typical ICM conditions, with magnetic field strengths of a few μG and downstream velocities $v_{\rm ds} \sim 10^3$ km s^{-1}, the radio emission at ∼1 GHz is expected to extend up to ∼50 kpc behind the shock front.

Regions with relatively flat spectral indices are therefore expected to lie close to the shock front, typically within a few tens of kiloparsecs. Selecting such regions may thus provide a practical way to isolate the immediate post-shock environment, particularly when the shock location cannot be robustly constrained from X-ray observations.

3.4. Promising targets in the search for NEI signatures

At $z \sim 0$, for gas near R_{500c}, the value of $\tau \sim 10^{12}$ cm^{-3} s corresponds to a timescale of ∼300 Myr. It is short enough to have a relatively small impact on the properties of an average cluster. Therefore, favorable conditions are needed to make the discussed features observable, such as ongoing mergers of massive, high-temperature clusters.

Here, we list several clusters that are promising targets for the search for nonequilibrium features.

- The Bullet cluster (1E 0657−56) at $z = 0.296$ provides a canonical example of a strong $\mathcal{M} \approx 3$ shock (Markevitch et al. 2002; Markevitch 2010). A combination of X-ray and Sunyaev-Zeldovich effect (SZ, Sunyaev & Zeldovich 1972) data provides hints of $T_e < T_p$ (Di Mascolo et al. 2019).
- El Gordo (ACT-CL J0102-4915) at $z = 0.87$ is another textbook example of merging galaxy clusters, a rare, massive system at high redshift (Menanteau et al. 2012). Numerical modeling suggests that it is observed close to the plane of the sky, with a shock Mach number of ∼4, approximately 100−200 Myr after pericentric passage (Zhang et al. 2015).
- The Peanut cluster (CL0238.3+2005) at $z \approx 0.42$, $kT \approx 10$ keV is a merger close to pericentric passage with a line-of-sight difference between the two subclusters of ∼2000 km s^{-1} (Lyskova et al. 2025; Zaznobin et al. 2026).
- Abell 2034 at $z \approx 0.113$ is a $kT \sim 8$ keV cluster undergoing a near plane-of-sky head-on merger. A prominent shock front lies ∼400 kpc from the cluster center (Owers et al. 2013; Monteiro-Oliveira et al. 2018). Heinrich et al. (2026) recently observed A2034 with *XRISM*, finding broader emission lines than those inferred in other clusters. There is also evidence that the Z/W ratio is low, which may indicate an NEI state of the line-emitting plasma. However, the current data yield a detection of this state at only $\lesssim 2\sigma$ significance. The Heα and Lyα emission lines are consistent with a $M \approx 1.8$ shock that heats the ICM from 6.5 keV to 12 keV. We show the evolution of the Z/W ratio for this shock in Figure 5 (right panel). The apparent ∼470 km/s velocity dispersion measured in this cluster could also be explained by a high Fe ion temperature of up to $T_Z \approx 85$ keV.
- MACS J0717.5+3745 at $z = 0.5458$, $kT \approx 12$ keV, with the suggested line-of-sight velocity difference of ∼3000 km s^{-1} (Adam et al. 2017).

4. Conclusions

We have examined the spectral signatures of nonequilibrium ionization and the inequality of the electron and ion temperatures in the ICM, arising from the propagation of merger shocks. In particular, we focused on the He-like iron triplet in hot plasma lacking Li-like ions and on the following features:

- The reduced ratio of the forbidden-to-resonance line Z/W, arising in plasma dominated by He- and H-like ions when the electron temperature increases suddenly. The duration of this phase is $t \sim 30\left(\frac{n_e}{10^{-3}\,{\rm cm}^{-3}}\right)^{-1}$ Myr. For the $\mathcal{M} \sim 3$ shock, this translates into a physical size of the region downstream of the shock of ∼50 kpc in a $kT \sim 10$ keV cluster (Fig. 5).
- On a similar timescale, He-like lines are boosted relative to H-like lines expected under CIE conditions for the $T_{\rm e}$ values derived from the shape of the observed continuum. This occurs due to the under-ionized state of plasma.
- Increased line broadening compared to expectations based on the $T_i = T_{\rm e}$ assumption is expected. If Coulomb scattering is the only mechanism that equilibrates the temperatures of different species, the lines can be very broad for $t \sim 30\left(\frac{n_e}{10^{-3}\,{\rm cm}^{-3}}\right)^{-1}$ Myr when $T_i > T_p > T_{\rm e}$, and moderately broad for $t \sim 300\left(\frac{n_e}{10^{-3}\,{\rm cm}^{-3}}\right)^{-1}$ Myr, when $T_i = T_p > T_{\rm e}$. Ignoring this effect might lead to an overestimation of the level of turbulence downstream of the shock (Fig. 6).
- The magnitude of these transient features in the X-ray spectra scales linearly with density, rather than the density squared, because the duration of the transient phase is inversely proportional to density (Sect. 3.1, Fig. 7).

These spectral signatures occur in addition to line shifts and broadening, as well as structures in the X-ray surface brightness due to the shock-generated discontinuities in the gas velocity and density, respectively. With the advent of the *XRISM* Observatory (Tashiro et al. 2025), it may become possible to identify shock-specific spectral signatures, enabling constraints on electron heating at the shock front and on temperature equilibration rates.

Acknowledgements. The work of Yu.R. was supported by NASA under award number 80GSFC24M0006. IK was supported by the Simons Foundation via the Simons Investigator Award to A. A. Schekochihin. CZ acknowledges the support of the Czech Science Foundation (GACR) Junior Star grant no. GM24-10599M. AH and IZ were partially supported by NASA grant number 80NSSC25K7693.

References

Adam, R., Bartalucci, I., Pratt, G. W., et al. 2017, A&A, 598, A115
Akahori, T., & Yoshikawa, K. 2010, PASJ, 62, 335
Bohdan, A., Pohl, M., Niemiec, J., et al. 2020, ApJ, 904, 12
Bykov, A. M., Paerels, F. B. S., & Petrosian, V. 2008, Space Sci. Rev., 134, 141
Caprioli, D., Orusa, L., Cernetic, M., Haggerty, C. C., & Ostler, B. 2025, ApJ, 993, L1
Chièze, J.-P., Alimi, J.-M., & Teyssier, R. 1998, ApJ, 495, 630
Churazov, E., Zhuravleva, I., Sazonov, S., & Sunyaev, R. 2010, Space Sci. Rev., 157, 193
Comerford, J. M., & Natarajan, P. 2007, MNRAS, 379, 190
Del Zanna, G., Dere, K. P., Young, P. R., & Landi, E. 2021, ApJ, 909, 38
Dere, K. P. 2007, A&A, 466, 771
Di Mascolo, L., Mroczkowski, T., Churazov, E., et al. 2019, A&A, 628, A100
Drury, L. O. 1983, Rep. Prog. Phys., 46, 973
Fox, D. C., & Loeb, A. 1997, ApJ, 491, 459
Ghavamian, P., Laming, J. M., & Rakowski, C. E. 2007, ApJ, 654, L69
Ghavamian, P., Schwartz, S. J., Mitchell, J., Masters, A., & Laming, J. M. 2013, Space Sci. Rev., 178, 633
Gu, M. F. 2008, Can. J. Phys., 86, 675
Hanusch, A., Liseykina, T. V., & Malkov, M. A. 2020, A&A, 642, A47
Heinrich, A., Zhuravleva, I., Zhang, C., et al. 2024, MNRAS, 528, 7274
Heinrich, A., Zhuravleva, I., Churazov, E., et al. 2026, OJAp, submitted [arXiv:2604.27161]
Inoue, S., Hayashida, K., Ueda, S., et al. 2016, PASJ, 68, S23
Khabibullin, I. I., & Sazonov, S. Y. 2012, Astron. Lett., 38, 443

Korreck, K. E., Zurbuchen, T. H., Lepri, S. T., & Raines, J. M. 2007, ApJ, 659, 773

Kramida, A., Ralchenko, Y., Reader, J., & NIST ASD Team 2024, NIST Atomic Spectra Database (ver. 5.12), [Online]. Available: https://physics.nist.gov/asd [2026, April 22]. National Institute of Standards and Technology, Gaithersburg, MD

Kunz, M. W., Schekochihin, A. A., Cowley, S. C., Binney, J. J., & Sanders, J. S. 2011, MNRAS, 410, 2446

Liedahl, D. A. 1999, in X-Ray Spectroscopy in Astrophysics, eds. J. van Paradijs, & J. A. M. Bleeker, 520, 189

Lodders, K., Palme, H., & Gail, H.-P. 2009, Landolt Börnstein, 4B, 712

Loi, F., Murgia, M., Govoni, F., et al. 2017, MNRAS, 472, 3605

Lyskova, N., Churazov, E., Khabibullin, I., et al. 2025, A&A, 693, A55

Markevitch, M. 2010, ArXiv e-prints [arXiv:1010.3660]

Markevitch, M., & Vikhlinin, A. 2007, Phys. Rep., 443, 1

Markevitch, M., Gonzalez, A. H., David, L., et al. 2002, ApJ, 567, L27

Menanteau, F., Hughes, J. P., Sifón, C., et al. 2012, ApJ, 748, 7

Mewe, R., & Schrijver, J. 1978, A&A, 65, 115

Monteiro-Oliveira, R., Cypriano, E. S., Vitorelli, A. Z., et al. 2018, MNRAS, 481, 1097

Norseth, C. T., Wik, D. R., Sarazin, C. L., Sun, M., & Gastaldello, F. 2025, ApJ, 992, 62

Oelgoetz, J., & Pradhan, A. K. 2004, MNRAS, 354, 1093

O'Neil, S., Barnes, D. J., Vogelsberger, M., & Diemer, B. 2021, MNRAS, 504, 4649

Owers, M. S., Nulsen, P. E. J., Couch, W. J., et al. 2013, ApJ, 780, 163

Porquet, D., Mewe, R., Dubau, J., Raassen, A. J. J., & Kaastra, J. S. 2001, A&A, 376, 1113

Prokhorov, D. A. 2010, A&A, 509, A29

Rajpurohit, K., Vazza, F., Hoeft, M., et al. 2020, A&A, 642, L13

Ralchenko, Y., & Maron, Y. 2001, J. Quant. Spectr. Rad. Transf., 71, 609

Raymond, J. C., Winkler, P. F., Blair, W. P., & Laming, J. M. 2017, ApJ, 851, 12

Raymond, J. C., Ghavamian, P., Bohdan, A., et al. 2023, ApJ, 949, 50

Russell, H. R., McNamara, B. R., Sanders, J. S., et al. 2012, MNRAS, 423, 236

Russell, H. R., Nulsen, P. E. J., Caprioli, D., et al. 2022, MNRAS, 514, 1477

Sarkar, A., Andrade-Santos, F., van Weeren, R. J., et al. 2024, ApJ, 962, 161

Sazonov, S. Y., Churazov, E. M., & Sunyaev, R. A. 2002, MNRAS, 333, 191

Schekochihin, A. A., & Cowley, S. C. 2006, Phys. Plasmas, 13, 056501

Spitzer, L. 1962, Physics of Fully Ionized Gases (New York: Interscience)

Sunyaev, R. A., & Zeldovich, Y. B. 1972, Comments Astrophys. Space Phys., 4, 173

Takizawa, M. 1999, ApJ, 520, 514

Tashiro, M., Kelley, R., Watanabe, S., et al. 2025, PASJ, 77, S1

Tsiolis, V., Spitkovsky, A., & Crumley, P. 2021, APS Meeting Abstracts, 2021, NO06.011

van Weeren, R. J., de Gasperin, F., Akamatsu, H., et al. 2019, Space Sci. Rev., 215, 16

Vink, J. 2012, A&ARv, 20, 49

Vink, J., Broersen, S., Bykov, A., & Gabici, S. 2015, A&A, 579, A13

Wilson, L. B., III, Chen, L.-J., Wang, S., et al. 2020, ApJ, 893, 22

Wong, K.-W., & Sarazin, C. L. 2009, ApJ, 707, 1141

XRISM Collaboration (Audard, M., et al.) 2025, ApJ, 985, L20

Yamaguchi, H., Eriksen, K. A., Badenes, C., et al. 2014, ApJ, 780, 136

Zaznobin, I., Lyskova, N., Bikmaev, I., et al. 2026, JHEAp, 53, 100632

Zhang, C., Yu, Q., & Lu, Y. 2015, ApJ, 813, 129

Zhuravleva, I., Churazov, E., Schekochihin, A. A., et al. 2019, Nat. Astron., 3, 832

Zuhone, J. A., & Roediger, E. 2016, J. Plasma Phys., 82, 535820301

Appendix A: NOMAD simulations

The calculations of ionization balances and line intensities were performed with the time-dependent collisional-radiative code NOMAD (Ralchenko & Maron 2001). The model includes ionization stages from Li-like Fe^{23+} to bare nucleus with the total number of levels of about 1700. In particular, the singly excited levels with $n \leq 10$ and doubly excited autoionizing levels $1snln'l'$ and $nln'l'$ with $n \leq 3$ and $n' \leq 5$ were included for Li- and He-like ions. The atomic data (e.g., energy levels, radiative transition probabilities, collisional cross sections, autoionization probabilities, etc.) for simulations were calculated using Flexible Atomic Code (Gu 2008) based on the relativistic model potential method.

In the first set of calculations, the evolution of the system of levels was determined from the rate equation:

$$\frac{d\hat{N}(t)}{dt} = \hat{A}(t) \cdot \hat{N}(t) \quad \text{(A.1)}$$

where $\hat{N}(t)$ is the vector of level populations over all ions ($\Sigma_i N_i(t) = 1$) and $\hat{A}(t)$ is the rate matrix. The initial condition $\hat{N}(t = 0)$ corresponds to the steady state equilibrium at $n_e = 10^{-3}\,\mathrm{cm}^{-3}$ and $T_e = 7\,\mathrm{keV}$. The time steps were chosen on a logarithmic scale via: $t_0 = 0$, $t_1 = 10^4$ s, and $t_{i+1} = t_i \cdot 1.2$ for $i = 1..169$ ($t_{169} = 2.408 \cdot 10^{17}$ s). At each time step between $i = 0$ and $i = 21$, the electron temperature increased by 1 keV until reaching 28 keV at $t_{21} = 3.834 \cdot 10^5$ s, after which it was kept constant. The calculated ion populations and line intensities for He-like and H-like lines are shown in Figs. 2 (open squares) and 4, respectively. The relative population influxes for Z and W lines are presented in Fig. A.1 while the absolute influxes are given in Fig. A.2. For the frozen ionization distribution at relatively small τ, an instantaneous increase of the electron temperature results in a mildly enhanced excitation influx for the W line. Although Z also experiences an increased influx due to the inner-shell ionization from the ground state of Fe^{23+}, the relatively small population of the latter cannot provide an influx increase comparable to that for W. Hence, the Z/W ratio decreases as compared to the low-temperature condition.

For the second set of calculations, the initial temperature (T_0) was set in the 1..50 keV range. Then, the temperature (T_1) was changing from 1 keV to 50 keV with a time step of 10^4 s. This time step is too short to modify abundances of the ions involved while long enough to ensure quasi-steady-state equilibration between the excited states within an ion, which is established on the times compared to the longest lifetimes (cf. $\tau \simeq 5 \cdot 10^{-9}\,\mathrm{s\,cm}^{-3}$ for the Z line). Then, the corresponding Z/W ratio was determined for the combination of (T_0, T_1) as shown in Fig. 3. After the fast rise of electron temperature, the contribution of the inner shell ionization from the ground state $1s^2 2s$ of the Li-like ion to the Z influx increases by about a factor of four and remains high until the progressive ionization begins to deplete Li-like ions at about $\tau \sim 10^{10}\,\mathrm{s\,cm}^{-3}$ (Figs. A.1 and A.2).

Appendix B: Reference list for the relevant lines

In Table B.1, we list key parameters of the lines considered in this study for reference.

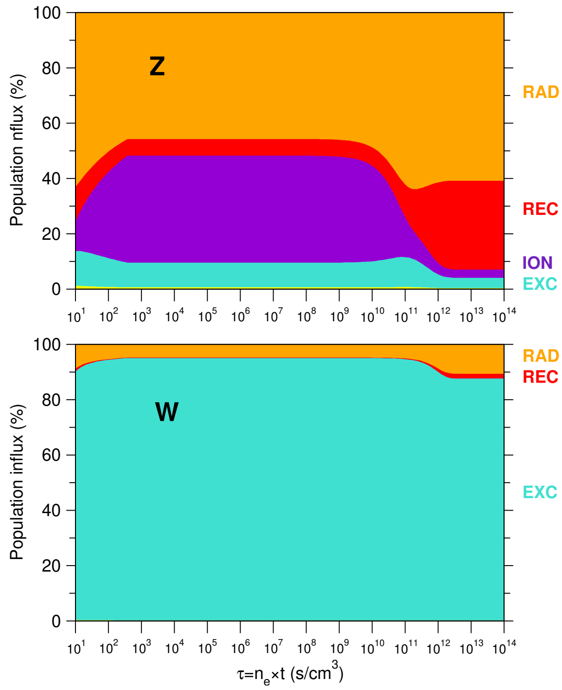

Fig. A.1. Relative population influxes for Z and W lines ($T_0 = 7$ keV, $T_1 = 28$ keV, $T_e = T_p$ case). RAD: radiative cascades, REC: direct radiative recombination from the H-like ground state, ION: inner shell ionization from the Li-like ion, EXC: electron-impact excitation.

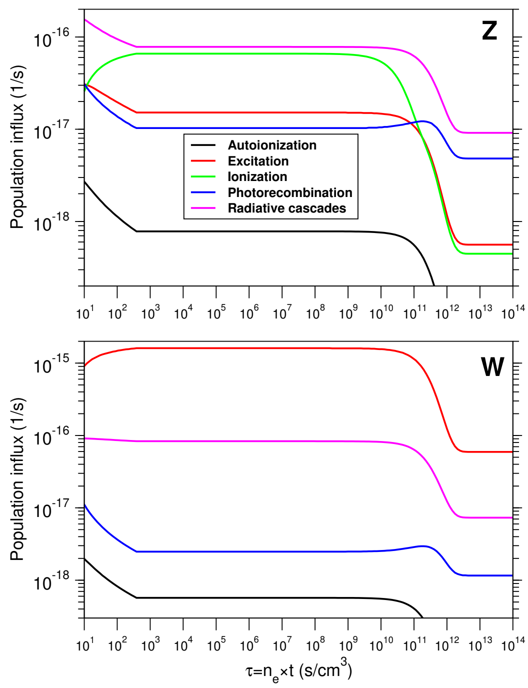

Fig. A.2. Absolute population influxes for Z and W lines ($T_0 = 7$ keV, $T_1 = 28$ keV, $T_e = T_p$ case).

Table B.1. Key parameters of the most relevant lines.

Spectroscopic symbol	Transition	Type	Energy, keV	Transition probability, s^{-1}
Fe XXV $K_\alpha - \mathtt{W}$	$1s^2\ ^1S_0$ - $1s2p\ ^1P_1$	E1	6.700	4.57×10^{14}
Fe XXV $K_\alpha - \mathtt{X}$	$1s^2\ ^1S_0$ - $1s2p\ ^3P_2$	M2	6.682	6.64×10^{9}
Fe XXV $K_\alpha - \mathtt{Y}$	$1s^2\ ^1S_0$ - $1s2p\ ^3P_1$	E1	6.668	4.42×10^{13}
Fe XXV $K_\alpha - \mathtt{Z}$	$1s^2\ ^1S_0$ - $1s2s\ ^3S_1$	M1	6.634	2.12×10^{8}
Fe XXVI $Ly\alpha_{3/2}$	$1s\ ^2S_{1/2}$ - $2p\ ^2P_{3/2}$	E1	6.973	2.8370×10^{14}
Fe XXVI $Ly\alpha_{1/2}$	$1s\ ^2S_{1/2}$ - $2p\ ^2P_{1/2}$	E1	6.952	2.8731×10^{14}

Notes. All data (energies rounded to 1 eV) are from NIST Atomic Spectra Database (Kramida et al. 2024).

Appendix C: Role of Helium in temperature equilibration

In this section, we verify the impact of helium on the ion temperature evolution, considering energy exchange between electrons, protons, helium ions, and ions of Fe XXV. The same assumption of a pure adiabatic heating of electrons at the shock is made. The subsequent evolution is mediated by Coulomb collisions. Fig. C.1 compares the evolution with helium (dashed lines) and without helium (solid lines). In the former case, the initial downstream temperature of ions is lower because of the increased mean atomic weight of plasma and, therefore, slower shock velocity (for the same upstream temperature and the shock Mach number), reducing the nonadiabatic heating of ions. Conversely, at later times ($\tau > 10^{12}$ cm^{-3} s), the presence of He ions keeps the Fe XXV ions slightly hotter, because He ions have the longest equilibration time scale.

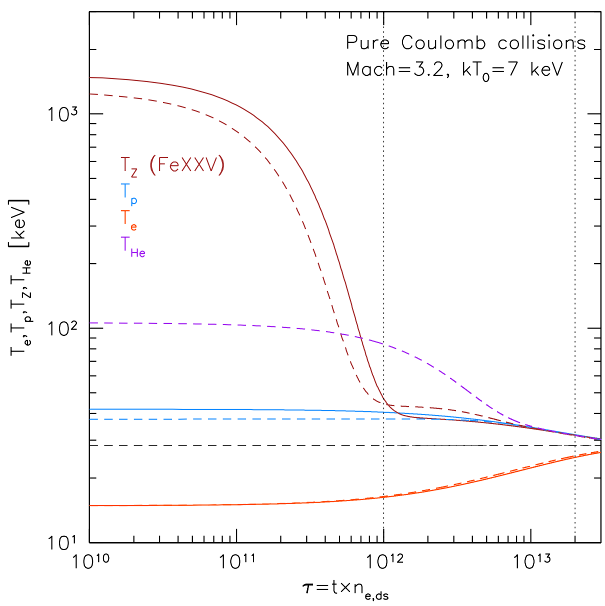

Fig. C.1. Impact of helium on the temperature equilibration. The solid lines correspond to the case with no helium, while the dashed lines show the temperature evolution when the He abundance is set to 0.084 of hydrogen (Lodders et al. 2009). The main effect of helium is (i) the increase of the mean atomic weight of plasma and, as a consequence, lower downstream temperature of ions (visible for $\tau < 10^{12}$ cm^{-3} s) and (ii) keeping Fe ions slightly hotter at $\tau > 10^{12}$ cm^{-3} s, since the helium ions have the longest equilibration time.